INORGANIC CHEMISTRY
FRONTIERS

RESEARCH ARTICLE

View Article Online
View Journal | View Issue



Cite this: *Inorg. Chem. Front.*, 2023, **10**, 2276

# Cu–Ni alloy decorating N-doped carbon nanosheets toward high-performance electrocatalysis of mildly acidic $CO_2$ reduction†

Weifan Pan,[a,b] Peng Wang,[a] Linfeng Fan,[a] Kai Chen,[a] Luocai Yi,[a] Junheng Huang,[a] Pingwei Cai,[a] Xi Liu,[a] Qingsong Chen,[a] Genxiang Wang*[a] and Zhenhai Wen*[a]

Electrochemical $CO_2$ reduction to value-added chemicals or fuels is a prospective strategy for facilitating the closing of the carbon loop. However, there still exist challenges in developing efficient catalysts and optimizing the electrolyzer components to meet industrial applications. Herein, nitrogen-doped "willow leaf" shaped carbon nanosheets modified with Cu–Ni alloy (CuNi-N-CNS) is designed for electrochemical $CO_2$ reduction reaction ($CO_2$RR), which shows high faradaic efficiency for CO of over 90% at a wide potential window ranging from −0.8 V to −1.0 V and robust durability with almost 100% of its initial selectivity after 36 h of electrolysis in H-type cell. Moreover, we evaluate its electrocatalytic activity in a self-assembly flow cell in a mildly acidic catholyte ($CO_2$-saturated 3 M KCl solution, pH = 4.25), which can achieve a commercially viable current density of 420 mA $cm^{-2}$ at −1.0 V *versus* reversible hydrogen electrode (*vs.* RHE) with CO selectivity above 95%. Experimental characterization and electrochemical analysis reveal that the synergistic effects of ultra-thin "willow leaf" structure and bimetallic alloy modification can not only increase electron transport efficiency but also decrease the reaction energy barrier of COOH* and promote the formation of CO.

Received 1st February 2023,
Accepted 6th March 2023

DOI: 10.1039/d3qi00207a

rsc.li/frontiers-inorganic



## Introduction

Massive carbon dioxide emissions from excessive utilization of fossil fuels have led to widespread environmental issues.[1–3] To date, many approaches have been adequately investigated to reduce the concentration of carbon dioxide in the atmosphere, among which electrocatalytic $CO_2$ reduction reaction ($CO_2$RR) driven by renewable electrical energy represents a realizable and convenient carbon-neutral pathway for producing valuable carbon-based chemical feedstocks.[4–6] However, the extremely stable C═O bond (806 kJ $mol^{-1}$) in $CO_2$ and the competing hydrogen evolution reaction in the aqueous phase hinder the activation of $CO_2$.[7,8] Besides, owing to the complex multiple proton and electron transfer processes during $CO_2$ reduction, the variety of products from $CO_2$ reduction adds extra difficulties in controlling its selectivity.[9–11] Among these possible products, CO is a more accessible product ($CO_2 + 2H^+ + 2e^- \rightarrow CO + H_2O$, −0.11 V *vs.* RHE) than other multi-carbon products in terms of reaction kinetics and is also an important raw material in industrial production.[12–14] Thus, elevating the conversion efficiency of $CO_2$ reduction into CO is crucial to promote the actual applications of $CO_2$RR.[15,16]

On one hand, designing effective catalysts for $CO_2$RR is still at the center of promoting the conversion efficiency of $CO_2$RR.[17,18] The electrocatalytic performance of catalysts is largely affected by their structure, crystal surface, and number of active sites.[19–21] Earlier, a variety of nano-structured Ag, Au, and Pd-based electrocatalysts have been studied due to their high selectivity and relatively low overpotential for $CO_2$ to CO in aqueous solutions.[22–25] But the scarcity of noble metals always limits their practical use. In this regard, replacing noble metal catalysts with non-noble carbon-based metal materials is a promising way towards sustainable $CO_2$RR.[26] Metal–organic framework-derived carbon-based materials hold great promise for applications in $CO_2$RR due to the exceptionally high surface areas, flexible electronic structure, multiple active sites, and designable morphology.[27,28] The single metal atom sites anchored on carbon materials derived from MOF templates have been widely prepared for $CO_2$RR and display excellent activity and selectivity for $CO_2$ reduction.[29] Compared with these carbon-based materials anchored with single sites,

[a]*CAS Key Laboratory of Design and Assembly of Functional Nanostructures, and Fujian Provincial Key Laboratory of Materials and Techniques toward Hydrogen Energy, Fujian Institute of Research on the Structure of Matter, Chinese Academy of Sciences, Fuzhou, Fujian, 350002, China. E-mail: wgx@fjirsm.ac.cn, wen@fjirsm.ac.cn*
[b]*University of Chinese Academy of Sciences, Bejing 100049, China*
†Electronic supplementary information (ESI) available. See DOI: https://doi.org/10.1039/d3qi00207a

carbon-based materials modified with metal alloys have received less attention but are still worthy of being studied owing to their rich components with tunable electronic structure and multicomponent cooperative effect.[30] For instance, Liu[31] reported ultrathin porous g-$C_3N_4$ nanosheets modified with AuCu alloy NPs catalyst. The charge transfer from Au to Cu in the alloy enriches Cu with excessive negative charges, which promotes the formation of intermediate *CO on the surface, thus increasing the yield of $C_2$ products. Roy's[32] group found that the carbon-supported PtZn nano-alloy can efficiently convert $CO_2$ to $CH_3OH$, resulting from the intermetallic alloy's ability to fine-tune electron transport properties and structures. Though desirable performance has been achieved on these reported carbon-based alloy catalysts, there is still room for designing other novel carbon-based catalysts with excellent catalytic performance.

On the other hand, the $CO_2$RR performance of catalysts is mainly investigated in H-cells or flow cells in neutral or alkaline electrolytes currently, where problems like $CO_2$ mass transport limitation, carbonation, and poor stability exist.[33] In these H-cells, the limited solubility and mass diffusion of $CO_2$ seriously limit its conversion rate.[15,34–36] In the widely reported gas diffusion electrode (GDE) based flow cells, the mass transport limitation problem can be avoided by constructing a gas–liquid–solid three-phase reaction interface, and the reaction rates are greatly improved.[37] However, the commonly used alkaline electrolyte and the high local pH of the reaction interface at large current density accelerate the carbonation and flooding of the flow cell, leading to poor stability and rather low $CO_2$ utilization.[38,39] In comparison, the $CO_2$RR performed in acidic media has emerged as a promising strategy to circumvent carbonation and its induced problems. Though hydrogen evolution reaction may be more favorable in acidic conditions, it can be suppressed by suitably adjusting the reaction interface of electrodes and the pH of the catholyte. For example, Sargent[40] carried out $CO_2$RR over copper in an electrolyte with pH < 1, which achieved a single-pass $CO_2$ utilization of 77% and a conversion efficiency of 50% toward multi-carbon products at a current density of 1.2 A $cm^{-2}$. Besides, Monteiro[41] investigated the feasibility of $CO_2$ electrolysis with 10 $cm^2$ gold gas diffusion electrodes at pH of 2–4, obtaining CO faradaic efficiencies between 80–90%, with a 30% improvement of the overall process energy efficiency in comparison with neutral media. The research of $CO_2$RR in acidic electrolytes opens up a unique routine for $CO_2$RR, and studying the $CO_2$RR performance of various catalysts in acidic electrolytes provides references for solving problems in practical applications of $CO_2$RR.[42–46]

Herein, we strategically design a nitrogen-doped "willow leaf" shaped carbon nanosheets modified with Cu–Ni alloy (CuNi-N-CNS) through a facile solvothermal-evaporation-pyrolysis process. The Cu–Ni alloy nanoparticles encapsulated in the *in situ* formed carbon layers decorate on the ultra-thin lancet nanosheets. Such a unique composite structure can greatly improve the catalytic activity for $CO_2$RR, which achieves a high CO faradaic efficiency of over 90% for $CO_2$ electroreduction at a potential window of −0.8 V to −1.0 V *vs.* RHE in H-Cell. Besides, the $CO_2$RR performance of the prepared catalyst was further investigated in a home-made flow cell with $CO_2$-saturated 3 M KCl solution as catholyte (pH = 4.25), which can provide a mildly acidic environment to prevent carbonation and achieve high current density (420 mA $cm^{-2}$) at −1.0 V with $FE_{CO}$ above 95%. Consequently, our study affords an innovative idea of designing metal-based catalysts for $CO_2$RR and provides the possibility for its industrialization.

## Results and discussion

### Catalyst preparation and characterization

As shown in Scheme 1, the catalyst was synthesized by a metal–organic framework (MOF) assisted method. The CuNi doped zeolitic imidazolate framework-8 (CuNi-ZIF-8) suspension was first fabricated by mixing zinc nitrate, copper nitrate, nickel nitrate, and 2-methylimidazole in DI water *via* vigorously stirring, and Resol-F127 solution was synthesized by heating phenolic resin and surfactant F127. Then, the nitrogen-doped ultra-thin carbon nanosheets modified with Cu–Ni alloy, named CuNi-N-CNS, were obtained *via* two steps of hydrothermal and pyrolysis reactions (for synthesis details, see ESI and Fig. S1, S2†). Remarkably, a gram-scale catalyst can be obtained *via* simply increasing feeding reagents (Fig. S3†) during synthetic processes, indicating the feasibility of scalable synthesis. For comparison, we probed the effect of raw material ratios on the structure of the CuNi-N-CNS catalyst to determine the optimal one. Ni-N-CNS, Cu-N-CNS, and N-CNS were also synthesized as controlled samples through a similar method (Fig. S2†).

The morphology characterizations of CuNi-N-CNS were conducted by scanning electron microscopy (SEM) and transmission electron microscopy (TEM). As displayed in Fig. 1a–c, the as-prepared catalyst maintained the uniform structure of ultra-thin "willow leaf" shaped nanosheets. In contrast, samples without Resol-F127 composite would lose the "willow leaf" structure and agglomerate after pyrolysis (Fig. S4†). It could be inferred that Resol-F127 played a crucial role in the whole reaction process. Specifically, in the hydrothermal process, Resol-F127 would attach to CuNi-ZIF-8 nanosheets due to the surface induction effect and cure with increasing temperature. Then, it *in situ* formed a carbon layer after undergoing the pyrolysis at 900 °C, which encapsulated Cu–Ni alloy nanoparticles, as revealed by the TEM images (Fig. 1d). In the HRTEM images of the calcined sample (Fig. 1e and f), the well-defined lattice streaks with *d*-spacings of 2.24 and 1.96 Å could be safely indexed to the (111) and (200) planes of Cu–Ni alloy, respectively. From the element mapping images (Fig. 1g), it can be demonstrated that Cu, Ni, C, and N species are homogeneously distributed in the carbon substrate, and CuNi alloy is clearly distributed on the surface. Complementally, as revealed by the inductively coupled plasma optical emission spectrometry (ICP-OES), the Cu and Ni contents of CuNi-N-CNS are determined to be 2.60 and 2.39 wt%, respectively. (Table S1†). EDS and XPS data are

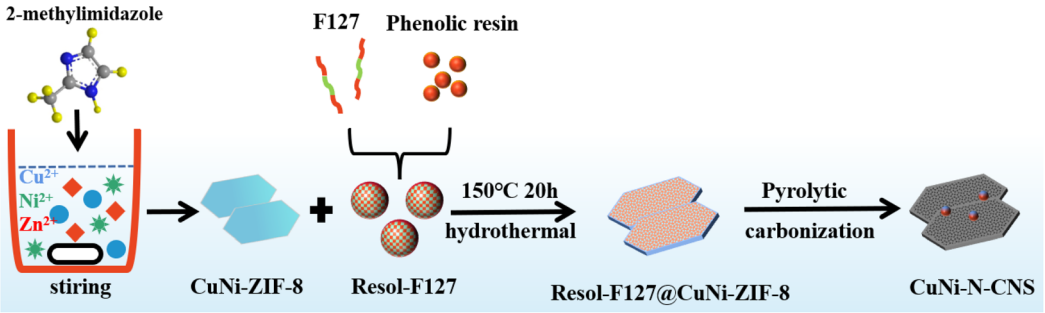


**Scheme 1** Schematic representation of the synthetic method of CuNi-N-CNS samples.

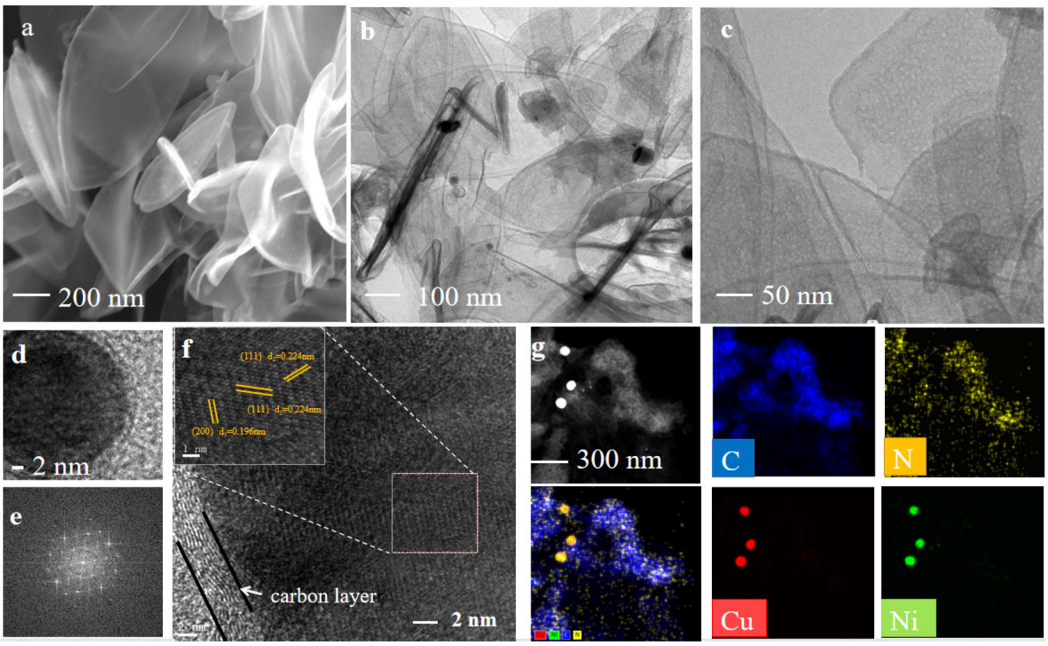


**Fig. 1** (a) High-resolution SEM patterns of CuNi-N-CNS. (b–c) TEM images of CuNi-N-CNS at different resolutions, and (d) CuNi@C in CuNi-N-CNS. (e) Corresponding FFT patterns. (f) HRTEM image and the enlarged image (g) EDS mapping of C, N, Cu, and Ni elements.



further used to assist in the determination of Cu and Ni contents (Fig. S5–S12†). The $N_2$ sorption isotherms (Fig. S13a†) further verify that the CuNi-N-CNS possesses a porous structure with a large specific surface area of 984.21 $m^2g^{-1}$. The pore size distribution (Fig. S13b†) peaks of the CuNi-N-CNS at *ca.* 0.68 nm (~2.1 times the dynamic diameter of $CO_2$ molecules) reveal its microporous structure, which could enhance the capture of $CO_2$, resulting in $CO_2$ enrichment around the active sites.

The X-ray diffraction (XRD) patterns exhibit that all as-prepared catalysts contain the characteristic peaks of carbon at 22° and 44° (Fig. S13d†). More concretely, CuNi-N-CNS display another three diffraction peaks at 43.6°, 50.8°, and 74.7°, which corresponded to the (111), (200), and (220) facets of $Cu_{0.81}Ni_{0.19}$ alloy (JCPSD no. 47-1406), respectively. For Ni-N-CNS and Cu-N-CNS, there are metallic Ni and Cu in the corresponding XRD patterns (Fig. S13d†). X-ray photoelectron spectroscopy (XPS) was then carried out to characterize the catalyst composition and elemental states on the surface (Fig. 2b). The high-resolution XPS N1s spectrum can be deconvoluted into pyridinic (~398.43 eV), M-N (~399.26 eV), pyrrolic (~400.92 eV), graphitic (~402.40 eV), and oxidized (~404.62 eV) species (Fig. 2c). In the high-resolution Ni 2p spectrum (Fig. 2d), the Ni $2p_{3/2}$ peak of CuNi-N-CNS can be fitted into the $Ni^0$ (855.03 eV) peak and $Ni^{2+}$ (856.39 eV) peak.[1,10–13] Moreover, the Cu 2p XPS spectrum in Fig. 2e reveals that the Cu $2p_{3/2}$ peak of CuNi-N-CNS can be fitted into $Cu/Cu^+$ (932.26 eV) peak and $Cu^{2+}$ (934.82 eV) peak.[1,13,17] Besides, the energy shift in the spectrum of CuNi-N-CNS compared with the single-metal and non-metal counterparts suggest the strong electronic effect between Cu and Ni atoms (Fig. S14–S17†). In Fig. 2f, Raman spectroscopy confirms the ratio of the defects and graphitization ($I_D/I_G$) with a D peak at 1351 $cm^{-1}$ and a G peak at 1580 $cm^{-1}$, respectively. The intensity ratio $I_D/I_G$ is widely used to indicate the activity and conductivity of the catalyst. Obviously, CuNi-C-CNS shows a relatively higher $I_D/I_G$

 

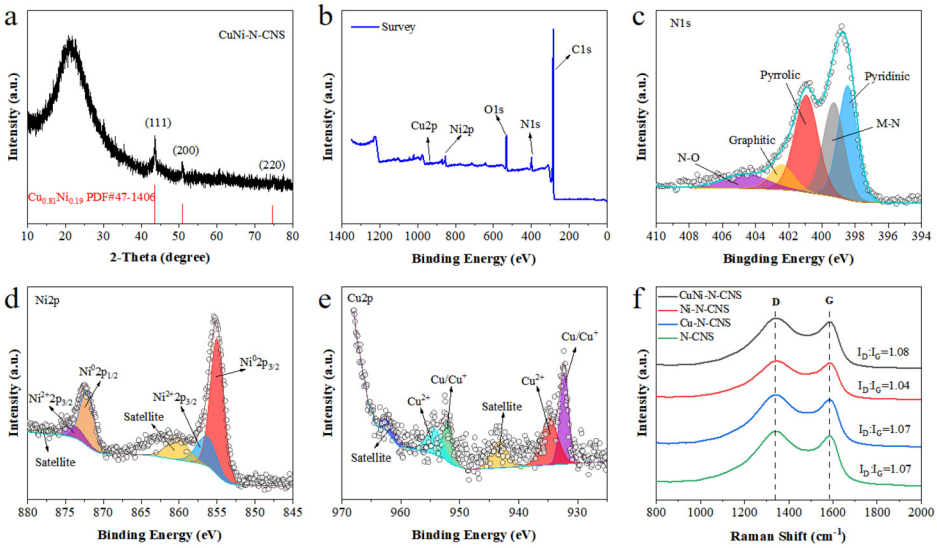


**Fig. 2** (a) X-ray diffraction patterns of CuNi-N-CNS. (b) The survey XPS spectrum of CuNi-N-CNS. (c–e) High-resolution spectra of N1s, Ni2p, and Cu2p of CuNi-N-CNS. (f) Raman spectra of CuNi-N-CNS, Ni-N-CNS, Cu-N-CNS, and N-CNS samples.

ratio of 1.08 in comparison with those of other counterparts. The higher D peak in CuNi-N-CNS could be essentially ascribed to the plentiful O cavities and a high level of defects, which resulted in increased active sites for improving $CO_2$RR performance.

These above characterization results reveal that the composite structure corresponds to carbon nanosheets with abundant Cu–Ni alloys wrapped in Cu/Ni–$N_x$–carbon (N–C@CuNi alloy) structure at the surface. For these CuNi-N-CNS catalysts, the Cu–Ni alloys cannot be effectively removed by acid etching due to the covering of the carbon layer. Although these embedded Cu–Ni alloys cannot directly involve the $CO_2$RR, the electronic interaction between Cu–Ni alloys and carbon nanosheets can enhance the activity of Cu/Ni–$N_x$–$C_y$ coordination for $CO_2$RR. Furthermore, recently reported works have suggested that the secondary metal Cu can not only positively shift the Ni 3d orbital energy to the Fermi level and thus accelerate the step of *COOH formation but also cause a considerable reaction barrier for water dissociation and thus decelerate the competing hydrogen evolution reaction.[1,13]

### Electrochemical performance for $CO_2$RR in H-cell

The electrocatalytic $CO_2$RR activity of the developed CuNi-N-CNS catalyst was first investigated in a typical H-cell with $CO_2$ saturated 0.5 M $KHCO_3$ solution as the electrolyte. For comparison, the $CO_2$RR activities of Ni-N-CNS, Cu-N-CNS, and N-CNS were also evaluated. As revealed by linear sweep voltammetry (LSV) curves in Fig. 3a, the CuNi-N-CNS exhibits a remarkably higher current density from −0.18 to −1.18 V *vs.* RHE compared with these controlled samples, giving current densities of 18 mA $cm^{-2}$ at −0.78 V and 42 mA $cm^{-2}$ at −1.18 V. Notably, the current density of CuNi-N-CNS increases faster than that of Ni-N-CNS at high potential, indicating the CuNi alloy may play a key role in elevating the conductivity of CuNi-N-CNS. Furthermore, the catalytic selectivity of these catalysts was also examined by the chronoamperometry technique. The gas and liquid products were monitored by gas chromatography (GC) and nuclear magnetic resonance (NMR), which indicated that CO and $H_2$ were the only two gas products of the reduction, and there was almost no liquid product (Fig. S18†). Fig. 3b compares the faradaic efficiency of CO ($FE_{CO}$) for these prepared catalysts in the potential range from −0.6 V to −1.1 V. Among them, CuNi-N-CNS exhibits impressively high selectivity (>90%) for CO at a wide potential window (−0.8 V to −1.0 V). While the peak $FE_{CO}$ of Cu-N-CNS and N-CNS are 58% and 10% at −0.7 V, far lower than that of CuNi-N-CNS. Fig. 3c shows the dependence of the CO partial current density ($j_{CO}$) on the applied potential. CuNi-N-CNS delivers much higher $j_{CO}$ with respect to the other catalysts and achieves a current density of 11 mA $cm^{-2}$ at −0.8 V, which is 1.2, 5, and 3 times higher than those of Ni-N-CNS, Cu-N-CNS, and N-CNS, respectively. The turnover frequency (TOF) of CO production for the developed CuNi-N-C catalyst was calculated based on the current density of $CO_2$RR and $FE_{CO}$, which exhibits an exceptionally high TOF of 879 $h^{-1}$ at −1.1 V, indicating the highly enhanced activity of bimetal-nitrogen sites. The Nyquist plot of CuNi-N-CNS exhibits the smallest semicircle among the prepared catalysts, which suggests its fast interfacial charge-transfer process during the $CO_2$RR process (Fig. 3d). Besides, to further compare the intrinsic activity of these catalysts, cyclic voltammetry (CV) measurements were performed to determine their electrochemical active surface areas (ECSAs) *via* the evaluation of double-layer capacitance ($C_{dl}$). CuNi-N-CNS showed the highest $C_{dl}$ of 244 mF $cm^{-2}$, which was 1.3, 1.5, and 2.4-fold of Ni-N-CNS, Cu-N-CNS, and N-CNS, respectively (Fig. S19†), verifying more active catalytic sites in CuNi-N-CNS. To uncover the reaction kinetics on different catalysts, Tafel plots were further determined and

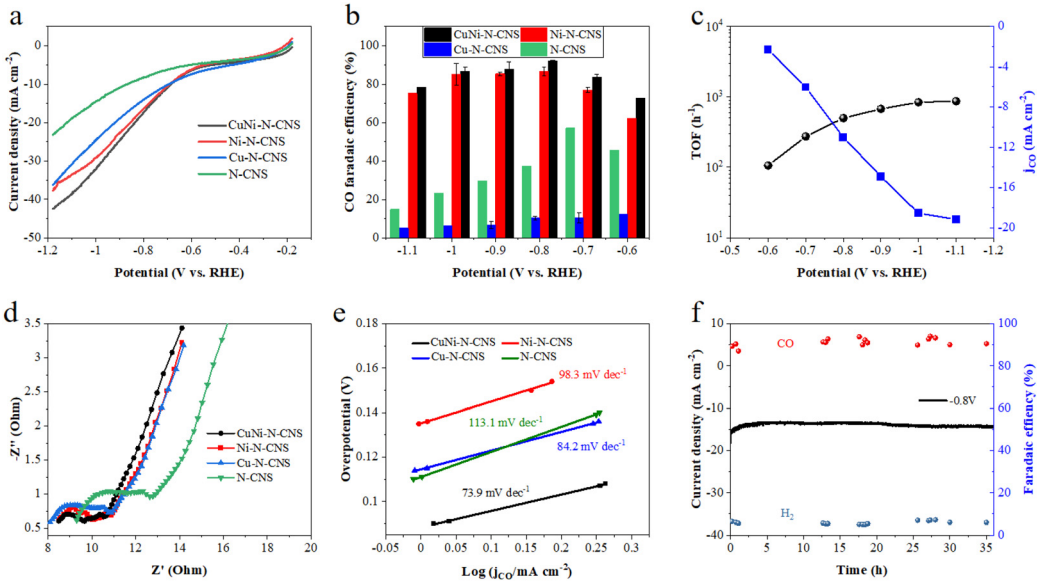


**Fig. 3** (a) LSV curves obtained in $CO_2$-saturated 0.5 M $KHCO_3$ solution (pH = 7.2) in the H-type cell. (b) faradaic efficiency for CO production at various applied potentials. (c) TOF of CuNi-N-CNS at various applied potentials. The blue curve is $j_{CO}$. (d) Nyquist plots. (e) Tafel plots of the samples. (f) Current–time response of CuNi-N-CNS on carbon paper for $CO_2$RR and the corresponding faradaic efficiency for CO/$H_2$ production at a fixed potential of −0.80 V (*versus* RHE).

analyzed. As shown in Fig. 3e, Tafel slopes of 73.9, 98.3, 84.2, and 113.1 mV decade$^{-1}$ are found over CuNi-N-CNS, Ni-N-CNS, Cu-N-CNS, and N-CNS, respectively. The lowest Tafel slope of CuNi-N-CNS further confirms its accelerated $CO_2$-to-CO conversion kinetics. Moreover, from the Tafel slope results, one can know that the first electron transfer ($CO_2 + H^+ + e^- \rightarrow$ *COOH), which generates surface adsorbed *COOH intermediate, is the rate-determining step for $CO_2$RR. The significantly lowered Tafel slope of CuNi-N-CNS indicates the kinetics of this step may be greatly enhanced. Beyond that, the CuNi-N-CNS also exhibits excellent durability for $CO_2$RR, maintaining almost 100% of the initial FE for CO production at −0.8 V after 36 h of continuous electrolysis in an H-type cell (Fig. 3f). The stability of the prepared catalyst was further confirmed by checking the SEM and XRD of the catalyst after long-term electrolysis. The XRD patterns of catalysts of similar mass before and after the stability test showed no obvious changes (Fig. S20,† peaks of $Cu_{0.81}Ni_{0.19}$ are not so observable owing to the very small amounts of samples). The SEM images of the sample after electrolysis also display the morphology is well preserved, and the element mapping of the post-reaction sample shows the homogeneous distribution of elements and the preservation of CuNi alloy particles (Fig. S20 and S21†). The above results confirmed the excellent stability of the prepared catalyst. The fact that the CuNi-N-CNS catalyst outperformed the counterparts clearly points out the crucial role of the bimetallic alloy in the reaction.

### Electrochemical performance in the flow cell

Given the $CO_2$ mass transfer limitation in H-type cells as well as the adverse impact of carbonation of $CO_2$RR in neutral or alkaline electrolytes, the $CO_2$RR performance of CuNi-N-CNS was further evaluated in a home-made flow cell with $CO_2$-saturated KCl aqueous as the cathode electrolyte to verify its practical application potential (Fig. 4a and Fig. S22†). The assembled flow cell is set up with CuNi-N-CNS as the cathode in $CO_2$-saturated 3 M KCl, a commercial RuIrTi mesh as the anode in 1 M KOH, an Ag/AgCl (saturated KCl aqueous solution) as the reference electrode in cathode chamber, and the Nafion 117 membrane as the separator. The use of a gas diffusion electrode can circumvent the transport limitation of $CO_2$, leading to a much higher current density of CuNi-N-CNS in the flow cell. To shed light on how electrolytes influence $CO_2$RR, the effects of different catholytes and concentrations on the flow cell performance were first explored.

As Fig. 4b displays, the CuNi-N-CNS in $CO_2$-saturated 0.5 M $KHCO_3$ aqueous solution presents a similar current density to that in 0.5 M KCl, and the current density significantly escalates from −152 mA cm$^{-2}$ to −700 mA cm$^{-2}$ with the KCl concentration increasing from 0.5 M to 3 M, which possibly results from that the high-concentration $K^+$ cations can promote ion exchange. Besides, the selectivity of the reaction products is regulated by the electrolyte (Fig. S23†). It is found that $Cl^-$ is much better at converting $CO_2$-to-CO than $HCO_3^-$ at the same concentration of $K^+$, and a highly concentrated solution of KCl can markedly improve the faradaic efficiency of CO while inhibiting hydrogen evolution.[47] More importantly, a mildly acidic environment that can efficiently avoid carbonation is formed by saturating KCl aqueous with $CO_2$. As shown in the inset of Fig. 4c, CuNi-N-CNS conveys a much smaller current density and higher onset potential in Ar-saturated KCl electrolyte compared with that in $CO_2$-saturated KCl, indicating a promising $CO_2$RR performance of CuNi-N-CNS in KCl

 

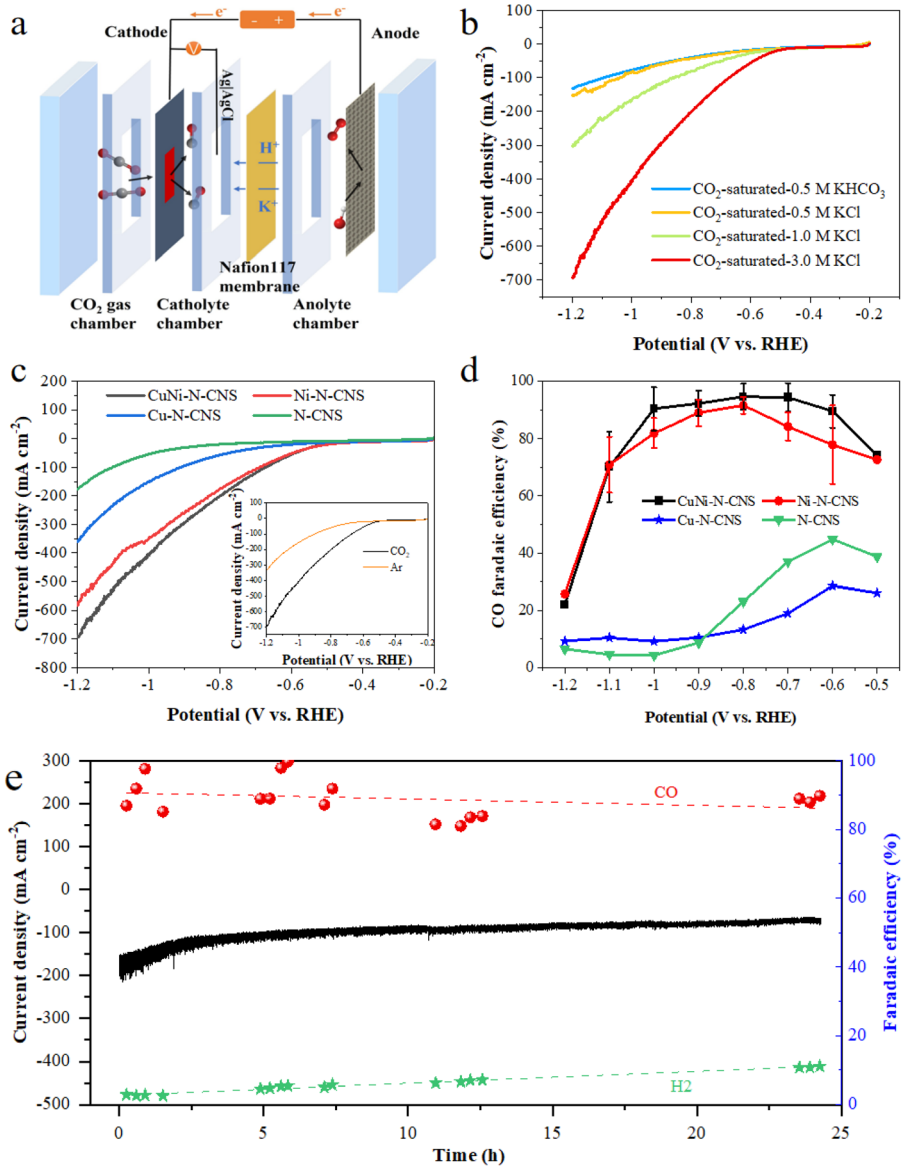


**Fig. 4** (a) Schematic diagram showing the basic structure of the flow cell that employs a gas diffusion electrode with the cathode electrolyte of 3 M KCl and the anode electrolyte of 1 M KOH. (b) LSV curves at a scan rate of 10 mV $s^{-1}$ with different cathode electrolytes. (c) LSV comparison for CuNi-N-CNS, Ni-N-CNS, Cu-N-CNS, and N-CNS. Inset: the LSV comparison for CuNi-N-CNS in Ar- and $CO_2$-saturated 3 M KCl solution. (d) $FE_{CO}$ as a function of potentials for CuNi-N-CNS, Ni-N-CNS, Cu-N-CNS, and N-CNS in the flow cell. (e) Stability assessment for CuNi-N-CNS at −0.8 V in the flow cell.

electrolyte. The $CO_2$RR performances of the controlled catalysts are also studied in the flow cell. The LSV curve trend of each sample in the flow cell is similar to those in H-cell. To be specific, the CuNi-N-CNS achieves a current density of 700 mA $cm^{-2}$ at −1.2 V *vs.* RHE, which is 1.2-fold, 2.0-fold, and 3.7-fold of Ni-N-CNS (570 mA $cm^{-2}$), Cu-N-CNS (355 mA $cm^{-2}$), and N-CNS (190 mA $cm^{-2}$), respectively (Fig. 4c). Besides, CuNi-N-CNS exhibits $FE_{CO}$ value over 90% in a wide potential ranging from −0.6 to −1.0 V, obviously superior to other counterparts (Fig. 4d). Moreover, we tested the long-term operation stability at −0.80 V as shown in Fig. 4e. The current density can maintain at above 100 mA $cm^{-2}$ during 24 h constant electrolysis with $FE_{CO}$ over 90%, which proves the satisfying performance under industrial high current density. Besides, when tested at 250 mA $cm^{-2}$, it can still maintain the perfect performance (Fig. S24†). It can be observed through the device diagram after a long-term test that the back of the carbon paper does not display serious flooding and salting out phenomenon, compared with that in the $KHCO_3$ electrolyte (Fig. S25†). Moreover, the existence of carbonate in the electrolyte is confirmed by the phenomenon of precipitation experiment, which shows a very small amount of precipitation occurring in the electrolyte after long-term electrolysis when the $BaCl_2$ solution was dropped into (Fig. S26†). We also tested the

catalyst performance in the flow cell of a two-electrode system. The LSV curve showed that the current density could reach 1260 mA $cm^{-2}$ at 3.8 V. Of course, under this condition, hydrogen production was preferred (Fig. S27 and S28†). While under a smaller cell voltage, $CO_2$RR was dominant, which exhibited a maximum $FE_{CO}$ of 94.14% at 2.2 V with a total current density of 180 mA $cm^{-2}$ (Fig. S29†), thus enabling $CO_2$ electrolysis at commercially relevant conditions ($j_{CO}$ > 100 mA $cm^{-2}$ and $E_{Cell}$ < 3 V).

## Conclusion

In summary, we have successfully designed a Cu–Ni alloy-modified carbon nanosheet catalyst for $CO_2$RR through a facile pyrolysis route, which owns a special "willow leaf" shaped structure. Multiple characterizations and experiments uncovered that the intermetallic CuNi alloy encapsulated with the N–C layer played an important role in regulating the electronic properties, thus accelerating *COOH adsorption and increasing the formation of CO. Benefiting from this, CuNi-N-CNS showed a high FE for CO of about 95% and a partial current density of about 400 mA $cm^{-2}$ at −1.0 V *vs.* RHE in a self-assembly flow cell using $CO_2$-saturated 3 M KCl solution as catholyte (pH = 4.25), which can also maintain good stability. This work not only affords new insights for the design of high-performance catalysts toward $CO_2$RR but also provides a reference for industrial application through optimizing the electrolyzer component parameters, especially by changing the electrolyte.

## Conflicts of interest

There are no conflicts to declare.

## Acknowledgements

This work was financially supported by the National key Research & Development Program of China (2022YFE0115900 and 2021YFA1501500), the National Natural Science Foundation of China (No. 22225902, U22A20436 and 22209183), the CAS-Commonwealth Scientific and Industrial Research Organization (CSIRO) Joint Research Projects (121835KYSB20200039), and the Joint Fund of the Yulin University and the Dalian National Laboratory for Clean Energy (Grant YLU-DNL Fund 2021011), Fujian Province Central Government Guides to Science and Technology Development Special Project (No. 2022L3024), and Fujian Natural Science Foundation (2021J01210293).

## References

1 J. Zhu, M. Xiao, D. Ren, R. Gao, X. Liu, Z. Zhang, D. Luo, W. Xing, D. Su, A. Yu and Z. Chen, Quasi-Covalently Coupled Ni-Cu Atomic Pair for Synergistic Electroreduction of $CO_2$, *J. Am. Chem. Soc.*, 2022, **144**, 9661–9671.

2 P. Ding, H. Zhao, T. Li, Y. Luo, G. Fan, G. Chen, S. Gao, X. Shi, S. Lu and X. Sun, Metal-based electrocatalytic conversion of $CO_2$ to formic acid/formate, *J. Mater. Chem. A*, 2020, **8**, 21947–21960.

3 G. Wang, J. Chen, K. Li, J. Huang, Y. Huang, Y. Liu, X. Hu, B. Zhao, L. Yi, T. W. Jones and Z. Wen, Cost-effective and durable electrocatalysts for Co-electrolysis of $CO_2$ conversion and glycerol upgrading, *Nano Energy*, 2022, **92**, 106751.

4 M. Chen, S. Wan, L. Zhong, D. Liu, H. Yang, C. Li, Z. Huang, C. Liu, J. Chen, H. Pan, D. S. Li, S. Li, Q. Yan and B. Liu, Dynamic Restructuring of Cu-Doped $SnS_2$ Nanoflowers for Highly Selective Electrochemical $CO_2$ Reduction to Formate, *Angew. Chem., Int. Ed.*, 2021, **60**, 26233–26237.

5 J. Li, A. Ozden, M. Wan, Y. Hu, F. Li, Y. Wang, R. R. Zamani, D. Ren, Z. Wang, Y. Xu, D. H. Nam, J. Wicks, B. Chen, X. Wang, M. Luo, M. Graetzel, F. Che, E. H. Sargent and D. Sinton, Silica-copper catalyst interfaces enable carbon-carbon coupling towards ethylene electrosynthesis, *Nat. Commun.*, 2021, **12**, 2808.

6 K. Li, J. Xu, T. Zheng, Y. Yuan, S. Liu, C. Shen, T. Jiang, J. Sun, Z. Liu, Y. Xu, M. Chuai, C. Xia and W. Chen, In Situ Dynamic Construction of a Copper Tin Sulfide Catalyst for High-Performance Electrochemical $CO_2$ Conversion to Formate, *ACS Catal.*, 2022, **12**, 9922–9932.

7 H. B. Yang, S.-F. Hung, S. Liu, K. Yuan, S. Miao, L. Zhang, X. Huang, H.-Y. Wang, W. Cai, R. Chen, J. Gao, X. Yang, W. Chen, Y. Huang, H. M. Chen, C. M. Li, T. Zhang and B. Liu, Atomically dispersed Ni(i) as the active site for electrochemical $CO_2$ reduction, *Nat. Energy*, 2018, **3**, 140–147.

8 T. Ahmad, S. Liu, M. Sajid, K. Li, M. Ali, L. Liu and W. Chen, Electrochemical $CO_2$ reduction to C2+products using Cu-based electrocatalysts: A review, *Nano Res. Energy*, 2022, **1**, e9120021.

9 W. Liu, S. Wei, P. Bai, C. Yang and L. Xu, Robust coal matrix intensifies electron/substrate interaction of nickel-nitrogen (Ni-N) active sites for efficient $CO_2$ electroreduction at industrial current density, *Appl. Catal., B*, 2021, **299**, 120661.

10 Y. Niu, C. Zhang, Y. Wang, D. Fang, L. Zhang and C. Wang, Confining Chainmail-Bearing Ni Nanoparticles in N-doped Carbon Nanotubes for Robust and Efficient Electroreduction of $CO_2$, *ChemSusChem*, 2021, **14**, 1140–1154.

11 L. Ji, L. Li, X. Ji, Y. Zhang, S. Mou, T. Wu, Q. Liu, B. Li, X. Zhu, Y. Luo, X. Shi, A. M. Asiri and X. Sun, Highly Selective Electrochemical Reduction of $CO_{(2)}$ to Alcohols on an FeP Nanoarray, *Angew. Chem., Int. Ed.*, 2020, **59**, 758–762.

12 W. Zhu, J. Fu, J. Liu, Y. Chen, X. Li, K. Huang, Y. Cai, Y. He, Y. Zhou, D. Su, J.-J. Zhu and Y. Lin, Tuning single atom-nanoparticle ratios of Ni-based catalysts for synthesis gas production from $CO_2$, *Appl. Catal., B*, 2020, **264**, 118502.

 

13 H. Cheng, X. Wu, M. Feng, X. Li, G. Lei, Z. Fan, D. Pan, F. Cui and G. He, Atomically Dispersed Ni/Cu Dual Sites for Boosting the $CO_2$ Reduction Reaction, *ACS Catal.*, 2021, **11**, 12673–12681.

14 H. Li, N. Zhang, S. Bai, L. Zhang, F. Lai, Y. Chen, X. Zhu and T. Liu, Strain-Regulated Pd/Cu Core/Shell Icosahedra for Tunable Syngas Electrosynthesis from $CO_2$, *Chem. Mater.*, 2022, **34**, 7995–8003.

15 Z.-Z. Niu, L.-P. Chi, R. Liu, Z. Chen and M.-R. Gao, Rigorous assessment of $CO_2$ electroreduction products in a flow cell, *Energy Environ. Sci.*, 2021, **14**, 4169–4176.

16 H. Yang, Y. Wu, Q. Lin, L. Fan, X. Chai, Q. Zhang, J. Liu, C. He and Z. Lin, Composition Tailoring via N and S Co-doping and Structure Tuning by Constructing Hierarchical Pores: Metal-Free Catalysts for High-Performance Electrochemical Reduction of $CO_2$, *Angew. Chem., Int. Ed.*, 2018, **57**, 15476–15480.

17 Z. Yin, H. Peng, X. Wei, H. Zhou, J. Gong, M. Huai, L. Xiao, G. Wang, J. Lu and L. Zhuang, An alkaline polymer electrolyte $CO_2$ electrolyzer operated with pure water, *Energy Environ. Sci.*, 2019, **12**, 2455–2462.

18 T. K. Todorova, M. W. Schreiber and M. Fontecave, Mechanistic Understanding of $CO_2$ Reduction Reaction ($CO_2$RR) Toward Multicarbon Products by Heterogeneous Copper-Based Catalysts, *ACS Catal.*, 2019, **10**, 1754–1768.

19 Q. Chen, K. Liu, Y. Zhou, X. Wang, K. Wu, H. Li, E. Pensa, J. Fu, M. Miyauchi, E. Cortes and M. Liu, Ordered Ag Nanoneedle Arrays with Enhanced Electrocatalytic $CO_2$ Reduction via Structure-Induced Inhibition of Hydrogen Evolution, *Nano Lett.*, 2022, **22**, 6276–6284.

20 H. Huo, J. Wang, Q. Fan, Y. Hu and J. Yang, Cu–MOFs Derived Porous Cu Nanoribbons with Strengthened Electric Field for Selective $CO_2$ Electroreduction to $C_{2+}$ Fuels, *Adv. Energy Mater.*, 2021, **11**, 2102447.

21 W. Wang, J. Han, Y. Sun, M. Zhang, S. Zhou, K. Zhao and J. Yuan, Metal-Free SeBN Ternary-Doped Porous Carbon as Efficient Electrocatalysts for $CO_2$ Reduction Reaction, *ACS Appl. Energy Mater.*, 2022, **5**, 10518–10525.

22 R. Zhao, P. Ding, P. Wei, L. Zhang, Q. Liu, Y. Luo, T. Li, S. Lu, X. Shi, S. Gao, A. M. Asiri, Z. Wang and X. Sun, Recent Progress in Electrocatalytic Methanation of $CO_2$ at Ambient Conditions, *Adv. Funct. Mater.*, 2021, **31**, 2009449.

23 Q. Chang, Y. Liu, J. H. Lee, D. Ologunagba, S. Hwang, Z. Xie, S. Kattel, J. H. Lee and J. G. Chen, Metal-Coordinated Phthalocyanines as Platform Molecules for Understanding Isolated Metal Sites in the Electrochemical Reduction of $CO_2$, *J. Am. Chem. Soc.*, 2022, **144**, 16131–16138.

24 R. Sui, J. Pei, J. Fang, X. Zhang, Y. Zhang, F. Wei, W. Chen, Z. Hu, S. Hu, W. Zhu and Z. Zhuang, Engineering Ag-Nx Single-Atom Sites on Porous Concave N-Doped Carbon for Boosting $CO_2$ Electroreduction, *ACS Appl. Mater. Interfaces*, 2021, **13**, 17736–17744.

25 S. Mou, Y. Li, L. Yue, J. Liang, Y. Luo, Q. Liu, T. Li, S. Lu, A. M. Asiri, X. Xiong, D. Ma and X. Sun, $Cu_2Sb$ decorated Cu nanowire arrays for selective electrocatalytic $CO_2$ to CO conversion, *Nano Res.*, 2021, **14**, 2831–2836.

26 Y. Cheng, S. Yang, S. P. Jiang and S. Wang, Supported Single Atoms as New Class of Catalysts for Electrochemical Reduction of Carbon Dioxide, *Small Methods*, 2019, **3**, 1970026.

27 Y. Zhao, L. Zheng, D. Jiang, W. Xia, X. Xu, Y. Yamauchi, J. Ge and J. Tang, Nanoengineering Metal-Organic Framework-Based Materials for Use in Electrochemical $CO_2$ Reduction Reactions, *Small*, 2021, **17**, e2006590.

28 Y. Zhu, X. Yang, C. Peng, C. Priest, Y. Mei and G. Wu, Carbon-Supported Single Metal Site Catalysts for Electrochemical $CO_2$ Reduction to CO and Beyond, *Small*, 2021, **17**, e2005148.

29 G. Wang, J. Chen, Y. Ding, P. Cai, L. Yi, Y. Li, C. Tu, Y. Hou, Z. Wen and L. Dai, Electrocatalysis for $CO_{(2)}$ conversion: from fundamentals to value-added products, *Chem. Soc. Rev.*, 2021, **50**, 4993–5061.

30 A. Jedidi, S. Rasul, D. Masih, L. Cavallo and K. Takanabe, Generation of Cu–In alloy surfaces from CuInO2as selective catalytic sites for $CO_2$ electroreduction, *J. Mater. Chem. A*, 2015, **3**, 19085–19092.

31 P. Li, L. Liu, W. An, H. Wang, H. Guo, Y. Liang and W. Cui, Ultrathin porous g-$C_3N_4$ nanosheets modified with AuCu alloy nanoparticles and C-C coupling photothermal catalytic reduction of CO to ethanol, *Appl. Catal., B*, 2020, **266**, 118618.

32 S. Payra, S. Shenoy, C. Chakraborty, K. Tarafder and S. Roy, Structure-Sensitive Electrocatalytic Reduction of $CO_2$ to Methanol over Carbon-Supported Intermetallic PtZn Nano-Alloys, *ACS Appl. Mater. Interfaces*, 2020, **12**, 19402–19414.

33 T. N. Nguyen and C. T. Dinh, Gas diffusion electrode design for electrochemical carbon dioxide reduction, *Chem. Soc. Rev.*, 2020, **49**, 7488–7504.

34 H. Yang, Q. Lin, C. Zhang, X. Yu, Z. Cheng, G. Li, Q. Hu, X. Ren, Q. Zhang, J. Liu and C. He, Carbon dioxide electroreduction on single-atom nickel decorated carbon membranes with industry compatible current densities, *Nat. Commun.*, 2020, **11**, 593.

35 Z. Xing, L. Hu, D. S. Ripatti, X. Hu and X. Feng, Enhancing carbon dioxide gas-diffusion electrolysis by creating a hydrophobic catalyst microenvironment, *Nat. Commun.*, 2021, **12**, 136.

36 K. Jiang, S. Siahrostami, T. Zheng, Y. Hu, S. Hwang, E. Stavitski, Y. Peng, J. Dynes, M. Gangisetty, D. Su, K. Attenkofer and H. Wang, Isolated Ni single atoms in graphene nanosheets for high-performance $CO_2$ reduction, *Energy Environ. Sci.*, 2018, **11**, 893–903.

37 C. Chen, X. Yan, Y. Wu, S. Liu, X. Zhang, X. Sun, Q. Zhu, H. Wu and B. Han, Boosting the Productivity of Electrochemical $CO_2$ Reduction to Multi-Carbon Products by Enhancing $CO_2$ Diffusion through Porous Organic Cage, *Angew. Chem., Int. Ed.*, 2022, **61**, e202202607.

38 Z. Chen, G. Yu, B. Li, X. Zhang, M. Jiao, N. Wang, X. Zhang and L. Liu, In Situ Carbon Encapsulation Confined Nickel-Doped Indium Oxide Nanocrystals for Boosting $CO_2$ Electroreduction to the Industrial Level, *ACS Catal.*, 2021, **11**, 14596–14604.

39 J. E. Huang, F. Li, A. Ozden, A. S. Rasouli, S. Zhang, M. Luo, X. Wang, D. Sinton and E. H. Sargent, $CO_2$ electrolysis to multicarbon products in strong acid, *Science*, 2021, **372**, 1074–1078.

40 M. C. O. Monteiro, M. F. Philips, K. J. P. Schouten and M. T. M. Koper, Efficiency and selectivity of $CO_2$ reduction to CO on gold gas diffusion electrodes in acidic media, *Nat. Commun.*, 2021, **12**, 4943.

41 J. Gu, S. Liu, W. Ni, W. Ren, S. Haussener and X. Hu, Modulating electric field distribution by alkali cations for $CO_2$ electroreduction in strongly acidic medium, *Nat. Catal.*, 2022, **5**, 268–276.

42 Y. Wu, K. Kamiya, T. Hashimoto, R. Sugimoto, T. Harada, K. Fujii and S. Nakanishi, Electrochemical $CO_2$ Reduction Using Gas Diffusion Electrode Loading Ni-doped Covalent Triazine Frameworks in Acidic Electrolytes, *Electrochemistry*, 2020, **88**, 359–364.

43 X. Zheng, P. De Luna, F. P. García de Arquer, B. Zhang, N. Becknell, M. B. Ross, Y. Li, M. N. Banis, Y. Li, M. Liu, O. Voznyy, C. T. Dinh, T. Zhuang, P. Stadler, Y. Cui, X. Du, P. Yang and E. H. Sargent, Sulfur-Modulated Tin Sites Enable Highly Selective Electrochemical Reduction of $CO_2$ to Formate, *Joule*, 2017, **1**, 794–805.

44 F. P. G. Arquer, C. T. Dinh, A. Ozden, J. Wicks, C. McCallum, D. Sinton and E. H. Sargent, $CO_2$ electrolysis to multicarbon products at activities greater than 1 A $cm^{-2}$, *Science*, 2020, **367**, 661–666.

45 H. Yano, T. Tanaka, M. Nakayama and K. Ogura, Selective electrochemical reduction of $CO_2$ to ethylene at a three-phase interface on copper(I) halide-confined Cu-mesh electrodes in acidic solutions of potassium halides, *J. Electroanal. Chem.*, 2004, **565**, 287–293.

46 Z. Wang, P. Hou, Y. Wang, X. Xiang and P. Kang, Acidic Electrochemical Reduction of $CO_2$ Using Nickel Nitride on Multiwalled Carbon Nanotube as Selective Catalyst, *ACS Sustainable Chem. Eng.*, 2019, **7**, 6106–6112.

47 Z. Zhao, J. Zhang, M. Lei and Y. Lum, Reviewing the impact of halides on electrochemical $CO_2$ reduction, *Nano Res. Energy*, 2023, **2**, e9120044.

 